ACS MATERIALS LETTERS

www.acsmaterialsletters.org

LETTER

Ionic Liquid-Mediated Intermediate Phase Adduct Constructing for Highly Stable Lead-Free Perovskite Solar Cells

Yuhan Zhou, Dongdong Yan, Han Zhang, Yi Jing, Linfeng Chao, Mingguang Li, Meicheng Li, Yonghua Chen,* Runfeng Chen,* and Ligang Xu*

Cite This: *ACS Materials Lett.* 2023, 5, 2096−2103

Read Online

ACCESS | Metrics & More | Article Recommendations | Supporting Information

ABSTRACT: **The intermediate phase adduct plays a crucial role in constructing uniform and compact tin perovskite films, thus providing an important approach for developing high-performance lead-free perovskite solar cells. However, the common intermediate phase adduct of SnI_2·3DMSO in tin perovskite leads to phase separation and may lack compatibility with mixed cation tin perovskites composed of formamidinium (FA) and methylamine (MA), impeding the further device stability. Here, a facile and reproducible method is developed to fabricate high-quality $FA_{0.75}MA_{0.25}SnI_3$ films by introducing a new stable intermediate phase adduct (SnI_2·DMSO·MAFa) by using ionic liquid methylamine formate (MAFa). The resulting stable adduct suppresses the reaction rate between ammonium salts and SnI_2, thereby modulating the tin perovskite crystallization and precluding SnI_2 clusters formation, and the presence of the SnI_2·DMSO·MAFa adduct in perovskite precursor serves as a protective barrier for Sn^{2+} ions, guarding them against oxidation caused by the presence of DMSO. Moreover, the amino and carbonyl groups in residual MAFa could repair the iodine vacancy and uncoordinated Sn^{2+} ion defects. These features result in the formation of highly uniform and pinhole-free $FA_{0.75}MA_{0.25}SnI_3$ films. The optimized devices achieve a power conversion efficiency (PCE) of over 10%, a value of 53% higher than that of the control device (6.6%). Besides, the obtained MAFa-derived devices illustrate significantly enhanced stability in a microaerobic atmosphere, with 78% maintained initial efficiency over 2800 h of storage under N_2 containing 50−100 ppm of O_2.**

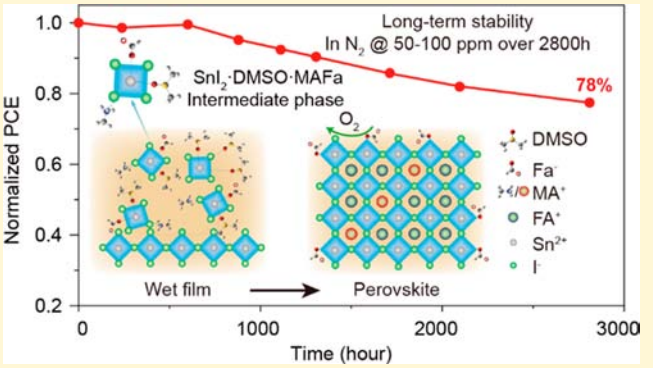

Lead-based perovskite solar cells have gained breathtaking development in the past decade, yielding power conversion efficiencies (PCE) up to 26.0%.[1−5] However, the involvement of toxic lead is a hinder for their commercialization.[6] To develop lead-free perovskites, various efforts have been made by replacing the Pb element with environmentally benign elements. Among various lead-free perovskites, tin perovskites are very promising, with PCEs increasing from 6.4% to 14.8%.[7,8] However, the fast crystallization of tin perovskites leads to poor film quality with highly formed defects.[9] Also, the easy oxidation of Sn^{2+} in tin perovskites induces p-type doping, leading to nonradioactive recombination loss and poor device performance.[10−12] As a result, tin-based perovskite solar cells (TPSCs) possess significantly inferior stability than lead-based PSCs.[13] To overcome these issues, tremendous efforts have been devoted to obtaining high-performance TPSCs via solvent engineering, perovskite composition adjustment, use of additives, and dimensional manipulation, among others.[14−16]

The hygroscopicity and low formation enthalpy of perovskite precursors require regulation of the crystallization process to yield uniform and smooth high-quality films.[17] Intermediate phases are often utilized to adjust the activation energy and crystallization kinetics to control the perovskite nucleation and growth.[18,19] In particular, the adduct approach based on Lewis base additives can form intermediate phases for high-quality homogeneous Sn perovskite films. Among Lewis acids, SnI_2

Received: April 4, 2023
Accepted: June 30, 2023
Published: July 6, 2023

https://doi.org/10.1021/acsmaterialslett.3c00340
ACS Materials Lett. 2023, 5, 2096−2103

could form intermediate-phase adducts through chemical interactions with Lewis bases.[20] For example, Kanatzidis et al. succeeded in reproducibly fabricating uniform and smooth $CH_3NH_2SnI_3$ films using the intermediate phase of SnI_2·3DMSO. Note that dimethyl sulfoxide (DMSO) with oxygen-bearing lone pair electrons could act as a Lewis base to form covalent bonds with SnI_2. As a result, SnI_2·3DMSO intermediate phase promotes homogeneous nucleation and delays the perovskite growth rate, resulting in high-quality perovskite films.[21] Nevertheless, the incompletely separated edge-sharing SnI_2 clusters caused by SnI_2·3DMSO intermediate phase in the precursor may lead to phase segregation, thus limited charge diffusion length and device stability,[22] and the DMSO/Sn^{2+} pair endures an irreversible redox reaction and generates dimethylsulfide (DMS) and Sn^{4+} in precursor.[23]

Meanwhile, SnI_2 as a stronger Lewis acid than PbI_2 may react with ammonium salts more quickly than its lead analogues.[24] Therefore, the tin perovskite crystallization can also be controlled by selecting suitable Lewis bases to form intermediate phase adducts. For instance, Li et al. regulated the crystallization of tin perovskite using BAAc ionic liquid to yield high-performance TPSCs with a PCE above 10%.[25] Dong et al. developed an ion exchange strategy by introducing an MA-based ion liquid into the $FASnI_3$ perovskite precursor to retard the crystallization process. The resulting lead-free TPSCs yielded a PCE of 8.5%.[26] However, the effects of ion liquid additives on the intermediate phases of the tin perovskite precursors have not yet been investigated. Besides, the superior optoelectronic and nontoxic properties of $FA_{0.75}MA_{0.25}SnI_3$ can be used to develop novel adduct approaches, allowing the formation of high-quality films for high-performance TPSCs.

Accordingly, an efficient method was developed in the present work to form highly uniform and reproducible $FA_{0.75}MA_{0.25}SnI_3$ films using the adduct approach. To this end, an ionic liquid of methylamine formate (MAFa, Figure S1 in the Supporting Information (SI)) was first utilized to form a new stable intermediate adduct phase with DMSO and SnI_2 (SnI_2·DMSO·MAFa) to preclude SnI_2 cluster formation in the precursor and slow down the rate of perovskite crystallization. Moreover, the presence of amino and carbonyl groups in MAFa repaired the iodine vacancy and uncoordinated the Sn^{2+} ion defects. Accordingly, a high PCE of 10.1% was achieved thanks to the highly uniform and smooth morphology of $FA_{0.75}MA_{0.25}SnI_3$. Most importantly, the MAFa-containing devices maintained approaching to ∼80% of the initial efficiency after 2800 h of storage under N_2 containing 50−100 ppm of O_2. The first introduction of a new intermediate phase adduct based ionic liquid, providing important progress in constructing high-quality tin perovskite films for highly stable lead-free perovskite solar cells.

Mechanism of MAFa in Perovskite Crystallization. In this study, MAFa ionic liquid was introduced into the precursor to form a new intermediate adduct phase for high-quality, lead-free perovskite films. Figure 1b schematically illustrates the formation process. For the tin perovskite precursor, the strong Lewis acidity of Sn^{2+} resulted in fast and uncontrollable crystallization (Figure 1a), generating many iodine vacancies and uncoordinated Sn^{2+} ions with low crystallinity. Meanwhile, residual SnI_2 was also induced in the tin perovskite films due to the formation of an intermediate phase adduct (SnI_2·3DMSO).[23] Numerous iodine vacancies were also formed owing to the rapid volatilization of DMSO, consistent with recent reports demonstrating the oxidation of Sn^{2+} to Sn^{4+} in

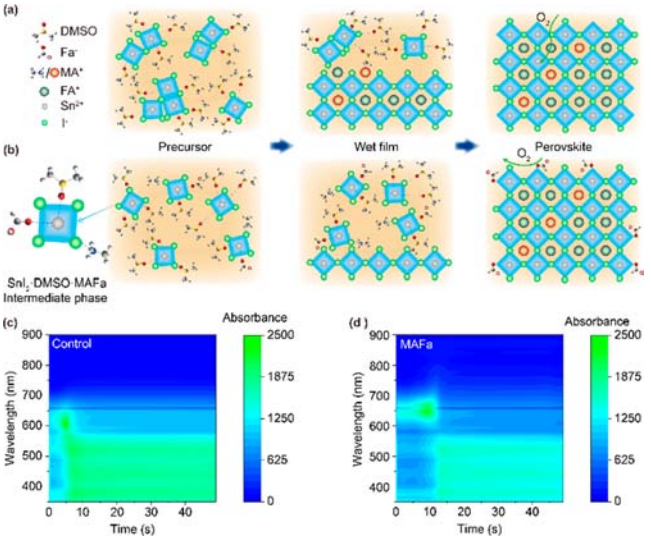

Figure 1. Schematic representation of the crystallization process of the (a) control and (b) MAFa-derived perovskite films. (c,d) *In situ* UV−vis absorption spectroscopy of control and MAFa-containing perovskite films.

solutions containing DMSO.[23,27] Thus, the general method without MAFa could induce inferior-quality films. By comparison, the introduction of MAFa in the perovskite precursor led to the formation of the SnI_2·DMSO·MAFa intermediate phase adduct thanks to C═O···Sn chemical interactions. The MA^+ also formed N−H···I hydrogen bonds between MAFa and I atoms of the tin perovskite. This resulted in a low crystallization rate, as proved by time-dependent photographs of wet perovskite films with and without MAFa (Figure S2 in the SI). The control film after the antisolvent engineering converted from a brown to black phase after 60 s, while MAFa-derived tin perovskite film still maintained the brown phase even after 100 s. From Figure S3 in the SI, the control precursor has a significant color change when annealing 120 °C for 1 h, while the MAFa-containing precursor shows no obvious change at the same condition. These results also proved that the SnI_2·DMSO·MAFa intermediate phase adduct can prevent the oxidation of Sn^{2+} in the precursor, which was induced by DMSO.

Characterization of Intermediate Phase Adduct. The crystallization process of the control and MAFa-containing perovskite was further studied by *in situ* ultraviolet−visible (*in situ* UV−vis) absorption spectroscopy, and the results are given in Figure 1c,d. The intensities in *in situ* UV−vis absorption spectra from 350 to 570 nm increased after annealing for 5 s for the control perovskite film, indicating the formation of tin perovskite.[28] By contrast, the time required to yield significantly improved intensity for MAFa-containing film absorption enlarged to 11.9 s, suggesting a reduced crystallization rate. Interestingly, a bump was observed between 570 and 650 nm for the control perovskite film, while a red-shift from 610 to 690 nm was noticed for MAFa-derived films. Also, the swelling disappeared with the rise in perovskite absorption, attributed to the existence of an intermediate phase adduct in the wet perovskite film. Note that MAFa-derived perovskites should have different intermediate-phase adducts to achieve high-quality tin perovskite films.

The electrostatic potential (ESP) is carried out to determine the charge distribution of MAFa. As shown in Figure S4 in the SI, abundant negative potential exists around the O atom of the

https://doi.org/10.1021/acsmaterialslett.3c00340
ACS Materials Lett. 2023, 5, 2096−2103

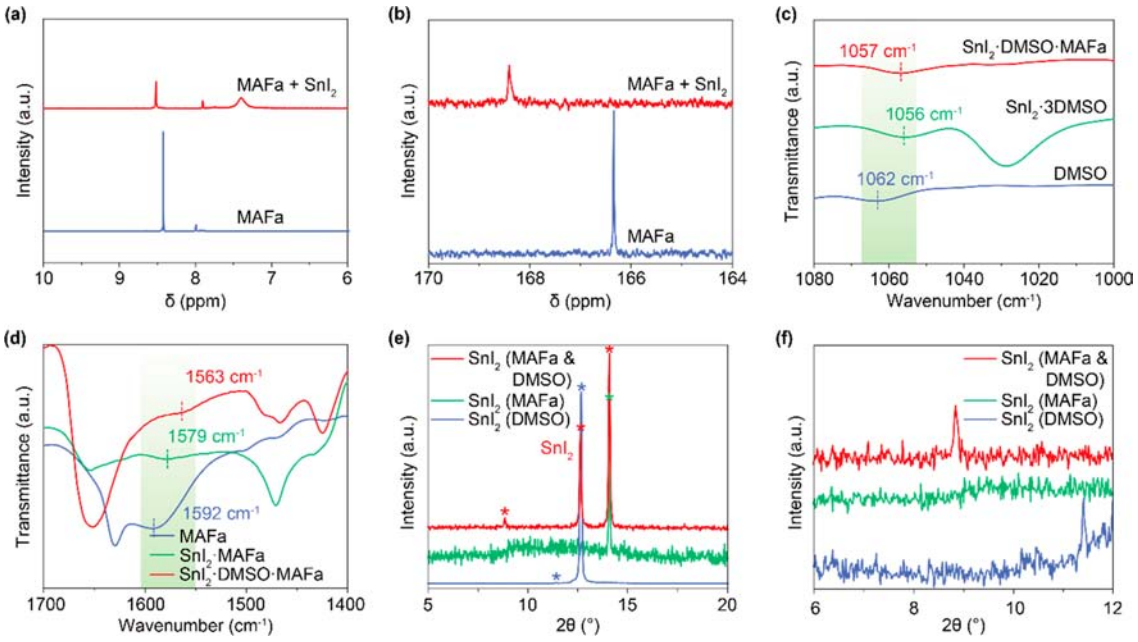

Figure 2. (a,b) ^{1}H NMR and ^{13}C NMR spectra of MAFa and MAFa + SnI_2 samples. (c) FTIR spectra of S═O peak, assigned to DMSO, SnI_2·3DMSO, and SnI_2·DMSO·MAFa C═O peak, respectively. (d) FTIR spectra of carbonyl peak, assigned to MAFa, SnI_2·MAFa, and SnI_2·DMSO·MAFa carbonyl peak, respectively. (e,f) XRD patterns of SnI_2 films prepared in DMSO, MAFa, and DMSO and MAFa mixed solvents, respectively.

Fa^- cation, indicating that Fa^- could be the most possible site that interacts with Sn^{2+} ions of perovskite. Then, to confirm the existence of the SnI_2·DMSO·MAFa intermediate phase adduct, nuclear magnetic resonance (NMR), and Fourier transform infrared (FTIR) spectrometry were carried out to verify the nature of adduct bonding (Figure 2a, and Figure S5 in the SI). The ^{1}H NMR spectra of MAFa and MAFa + SnI_2 samples revealed the presence of chemical shifts in the ammonium group of the MAFa peak at 8.0 to 7.9 and 7.4 ppm (Figure 2a). The aliphatic protons with the resonance signals at high field showed the same shifting direction as ammonium protons (Figure S5 in the SI). Thus, the N−H···I hydrogen bonds were formed between the MA^+ cation and the I^-site halogen anion. The resonance signal shifting from 8.4 to 8.5 ppm can be attributed to the protons of the Fa^- anion. This contrasting chemical shift primarily arises from electron delocalization induced by the coordination between the carbonyl group (C═O) and Sn^{2+}. The ^{13}C NMR was also characterized to investigate the interaction between Fa^- and SnI_2. As shown in Figure 2b, the resonance signals of the carbonyl group in MAFa shifted from 166.3 to 168.4 ppm (MAFa + SnI_2), indicating carbon of the carbonyl group losing some electron density due to the coordination interaction between the oxygen atom of MAFa and Sn atom in tin perovskite.[25]

For comparison, different adducts of SnI_2·3DMSO, SnI_2·MAFa, and SnI_2·DMSO·MAFa were also prepared, and their FTIR spectra were used to investigate the bonding nature of their corresponding adducts (Figure 2c,d). The S═O stretching vibration peak of DMSO in Figure 2c was recorded at around 1062 cm^{-1}, while it shifted to 1056 cm^{-1} after SnI_2·3DMSO adduct formation (Figure 2c). This can be explained by the S═O bond sharing the lone pair electrons in oxygen with SnI_2, thereby weakening the strength of the bond and reducing the stretching vibration frequency.[29] Interestingly, the corresponding stretching vibration peak of SnI_2·DMSO·MAFa changed to 1057 cm^{-1} after the introduction of the MAFa ion liquid, indicating changes in the electronic environment of S═O prone to the formation of new adducts. The C═O stretching vibration peak of MAFa in Figure 2d was recorded at 1592 cm^{-1} attributed to the Fa^- anion, while the peak shifted to 1579 cm^{-1} for SnI_2·MAFa. The C═O bond of the SnI_2·DMSO·MAFa adduct showed further red-shifting to 1563 cm^{-1} due to changes in the long pair electrons of C═O in MAFa. Therefore, MAFa formed a coordinative bond with SnI_2·3DMSO to generate a new adduct SnI_2·DMSO·MAFa.

The wet SnI_2 films prepared in different solvents (DMSO, MAFa, and DMSO and MAFa mixed solvents) were characterized by X-ray diffraction (XRD), and the data are provided in Figure 2e,f. The SnI_2 film based on DMSO exhibited a strong SnI_2 diffraction peak at 12.4°, indicating strongly separated edge-sharing SnI_2 clusters associated with SnI_2·3DMSO.[22] By comparison, the SnI_2 film prepared by MAFa and DMSO mixed solvent (1:1 v:v) showed a new peak at 8.8°, correlated with the SnI_2·DMSO·MAFa adduct. The small amount of MAFa resulted in two kinds of intermediate phase adducts (SnI_2·3DMSO and SnI_2·DMSO·MAFa) in the precursor due to the small induced amount of MAFa (5 mol %). However, the film prepared by bare MAFa showed only a peak at 2θ = 14.08° without other peaks, close to the (100) crystal plane of $FA_{0.75}MA_{0.25}SnI_3$ (14.02°). This can be explained by the reaction of MAFa with SnI_2 to form a similar perovskite structure.[30]

Tin-Based Perovskite Films. The influence of the SnI_2·DMSO·MAFa adduct on the crystallization of tin perovskite film was studied by XRD. As displayed in Figure S6 in the SI, the wet perovskite film before antisolvent engineering and thermal annealing showed an XRD peak at 2θ = 12.4° associated with SnI_2 due to phase segregation caused by the incompletely separated edge-sharing SnI_2 clusters. However, the wet perovskite film based on the SnI_2·3DMSO·MAFa adduct displayed no SnI_2 diffraction peak, suggesting the contribution of the new intermediate phase to precluding the SnI_2 cluster in the

https://doi.org/10.1021/acsmaterialslett.3c00340
ACS Materials Lett. 2023, 5, 2096−2103

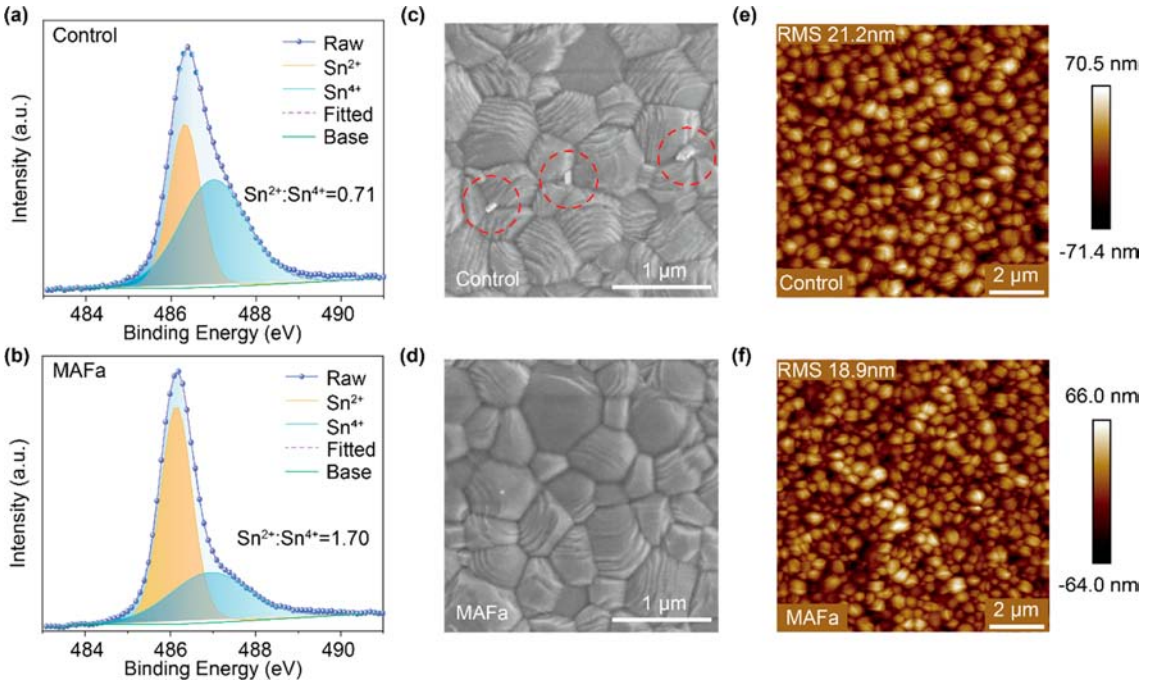

Figure 3. (a,b) Sn XPS spectra of the control and MAFa-containing perovskite films. (c,d) SEM images of the control and MAFa-containing perovskite. (e,f) AFM images of the control and MAFa-containing perovskite.

precursor (Figure S6a in the SI). After chlorobenzene dripping and thermal annealing, the MAFa-derived perovskite film shows significantly enhanced (h00) plane peak intensity, consistent with the XRD patterns of wet films (Figure S6b in the SI). Meanwhile, the full width at half-maximum (fwhm) of the (100) plane in Figure S6cin the SI revealed a lower value of MAFa-derived perovskite film than the control film. Hence, MAFa induced a better crystallization with a larger crystallite size.[31] The SnI_2·DMSO·MAFa intermediate phase adduct promoted perovskite growth along the vertical [100] direction, beneficial for reducing charge transport for higher device performance.

To confirm the perovskite crystal quality, the absorption spectra of the control and MAFa-containing perovskite films were further characterized, and the data are given in Figure S7a in the SI. The Tauc plots in Figure S7b in the SI suggested the same bandgaps of control and MAFa-derived perovskite films (1.34 eV). As a result, MAFa may only exist at grain boundaries and not in lattice bulk.[32] The residual MAFa in the grain boundaries can prevent the oxidation of Sn^{2+}, which is conducive to improving the device stability. The color change of the perovskite precursor aged at 48 h can confirm the absence of Sn^{2+} oxidation due to introduction of MAFa (Figure S8 in the SI). The Sn^{4+} content was further studied by X-ray photoelectron spectroscopy (XPS). As shown in Figure 3a,b, the Sn^{2+}:Sn^{4+} ratio increased from 0.71 to 1.70, suggesting remarkably suppressed oxidation of Sn^{2+}. As shown in Figure S9 in the SI, the C═O stretching vibration peak of MAFa-derived perovskite was recorded at around 1579 cm^{-1}, which was consistent with the FTIR spectra of SnI_2·DMSO·MAFa (Figure 2d). Thus, MAFa can remain in the perovskite to repair the iodine vacancy and uncoordinated Sn^{2+} ion defects. The compact MAFa-containing perovskite film prevented water and oxygen from entering into the film due to the encapsulation by the residual MAFa in grain boundaries.

The morphologies of perovskites based on different intermediate phase adducts were further explored by scanning electron microscopy (SEM) and atomic force microscopy (AFM), and the data are summarized in Figure 3c,f. For the control perovskite film, some SnI_2 clusters were visible on the surface, with an average grain size of 0.48 μm (Figure S10a in the SI). By comparison, the SnI_2 clusters disappeared in MAFa-derived film showing a larger average grain size (0.50 μm, Figure S10b in the SI). Therefore, the SnI_2·DMSO·MAFa adduct could preclude the SnI_2 cluster. Based on AFM images (Figure 3e,f), the root mean surface (RMS) roughness of MAFa-derived perovskite films was 18.9, which is lower than that of the control film (21.2). Therefore, MAFa induced better-quality perovskite films in comparison to the control precursor.

Device Performance of TPSCs. The promising above findings related to MAFa-derived tin perovskite films encouraged the fabrication of inverted TPSCs (0.09 cm^2) with the device structure ITO/PEDOT:PSS/$FA_{0.75}MA_{0.25}SnI_3$/C_{60}/BCP/Al (Figure S11 in the SI). As depicted in the current-density voltage (J−V) curves (Figure 4a, and Table S1 in the SI), the control device without MAFa exhibited a PCE of 6.6% under forward scan and short-circuit current density (J_{sc}) of 21.9 mA cm^{-2}, with V_{oc} of 0.58 V and fill factor (FF) of 0.52. By comparison, TPSCs based on 5 mol % MAFa displayed an improved PCE up to 10.1%, with J_{sc} of 22.4 mA cm^{-2}, V_{oc} of 0.69 V, and fill factor (FF) of 0.63. The J−V curves in both reverse and forward scans revealed a smaller hysteresis index (HI, 0.041) of the MAFa-derived device than that of the control device (0.078), suggesting suppression of the ion migration in residual MAFa due to the chemical interactions with the perovskite defects. The external quantum efficiency (EQE) of MAFa-based TPSCs in Figure 4b indicated an integrated J_{sc} (21.61 mA cm^{-2}) value consistent with the J−V curves (22.4 mA cm^{-2}). Also, the MAFa-based device showed an enhanced light utilization in the range of 300−500 nm, consistent with UV−vis spectrometry. The statistics of PCEs distributions for the corresponding devices are summarized in Figure 4c. A total of 20 devices with and without MAFa were fabricated, and the

https://doi.org/10.1021/acsmaterialslett.3c00340
ACS Materials Lett. 2023, 5, 2096−2103

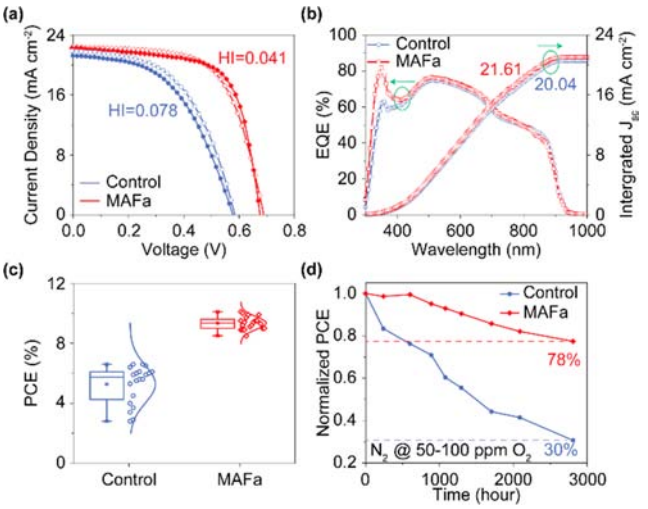

Figure 4. (a) $J-V$ curves of the control and MAFa-containing TPSCs under both reverse and forward voltage scans. (b) EQE and integrated J_{sc} of the control and MAFa-containing TPSCs. (c) Statistics of PCEs distribution for the control and MAFa-containing devices. (d) PCEs storage stability of unencapsulated devices under N_2 containing 50−100 ppm of O_2.

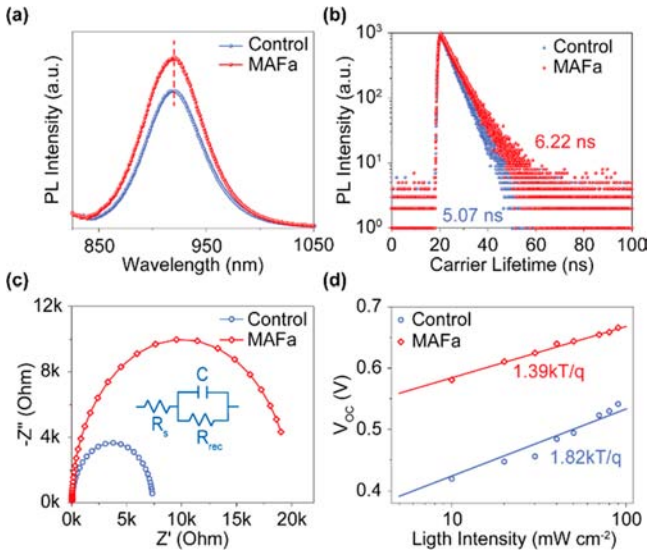

Figure 5. (a,b) PL and PL decay spectra of the control and MAFa-containing perovskite film. (c) Nyquist plots of the control and MAFa-containing PSCs. (d) Light-intensity-dependent V_{oc} curves of the control and MAFa-containing PSCs.

measured parameters J_{sc}, V_{oc}, and FF are provided in Figure S12 in the SI. Obviously, intermediate phase SnI_2·DMSO·MAFa significantly improved the device reproducibility and performance.

The long-term stability of the unencapsulated control and MAFa-derived TPSCs was investigated under a N_2 atmosphere containing 50−100 ppm of O_2 (Figure 4d). The control TPSCs showed a decreased PCE to 30% of the initial value after 2808 h of aging. By comparison, the MAFa-derived TPSCs maintained ∼80% of the initial PCE under the same conditions, suggesting strong improvement. The details of the photovoltaic parameters (J_{sc}, V_{oc}, and FF) are exhibited in Figure S13 in the SI. The degradations in both FF and J_{sc} of the control TPSCs were also much faster than those of the MAFa-derived device. Also, MAFa-derived devices have more stable V_{oc}, which is associated with defects in perovskite, and MAFa can repair the iodine vacancy and uncoordinated Sn^{2+} ion defects. Afterward, the stability of the corresponding unencapsulated TPSCs was tested in air with RH ≈ 65%. Here, the aluminum electrode was replaced by a copper electrode due to its poor stability under high humidity (Figure S14a in the SI). The MAFa-derived TPSCs illustrated no obvious degradation after 180 min of aging in air, whereas the control TPSCs significantly dropped to ∼20% of the initial PCE after 100 min storage (Figure S14b in the SI). The improved stability was linked to the high-quality tin perovskite films and the chemical interactions between MAFa and perovskite. The air stability originated from the reduction of the aldehyde group in the Fa^- anion, which can protect Sn^{2+} from O_2 oxidation. Moreover, MAFa also improved the hydrophobicity of the tin perovskite (Figure S15 in the SI), leading to enhanced air stability.

Charge Dynamics. The charge dynamics of the MAFa-derived tin perovskites were investigated by steady-state photoluminescence (PL) and PL decay spectroscopy (Figure 5a,b). The PL peak wavelengths of both control and MAFa-containing perovskites did not change, consistent with the bandgaps obtained from Tauc plots (Figure S5b in the SI). Moreover, the PL intensity of MAFa-derived perovskite was significantly increased when compared to that of the control sample, suggesting high-quality tin perovskite films with reduced defects formed by MAFa. The PL decay spectra revealed a prolonged photogenerated carrier lifetime of MAFa-derived perovskite films from 5.07 to 6.22 ns, indicating suppression of charge recombination. Furthermore, the SnI_2·DMSO·MAFa intermediate phase adduct contributed to the reduction of the leakage current, leading to a decreased background carrier density (Figure S16 in the SI).

The charge recombination was further investigated by electrochemical impedance spectroscopy (EIS) at 0.6 V. As shown in Figure 5c, the Nyquist plots of both devices displayed the main arc related to the recombination resistance values (R_{rec}).[33] The R_{rec} of the MAFa-based TPSC increased by 161% compared to that of the control device. Thus, the MAFa-derived perovskite possessed a lower recombination rate.

To clarify the trap-assisted charge recombination, the light-intensity-dependent V_{oc} curves of the control and MAFa-derived devices were obtained. As depicted in Figure 5d, the ideal factor of the MAFa-based TPSC revealed light-intensity-dependent V_{oc} curves reduced from 1.82 to 1.39, suggesting significantly declined Shockley−Read−Hall recombination in MAFa-based TPSCs.[34] Thus, the space-charge-limited current (SCLC) was analyzed for the corresponding hole-only devices to calculate the trap state density. In Figure S17 in the SI, the dark $J-V$ curves can be divided into three regions: omega region, trap filling limit region, and child region. The trap filling limit voltages (V_{TFL}) were obtained from SCLC to calculate the defect density inside the films.[35,36]

$$N_{dt} = \frac{2\varepsilon\varepsilon_0 V_{TFL}}{eL^2}$$

where ε and ε_0 represent the relative dielectric constant and vacuum permittivity, respectively. q and L are elementary charge and perovskite thin film thickness.

The trap-filling limit voltages of the control and MAFa-based device were estimated to 1.65 and 0.84 eV, respectively. The corresponding hole trap state densities were 2.63×10^{17} and 1.35×10^{17} cm^{-3}, respectively. These data further confirmed

https://doi.org/10.1021/acsmaterialslett.3c00340
ACS Materials Lett. 2023, 5, 2096−2103

that the MAFa could induce high-quality tin perovskite films as well as contribute to the reparation of defects through chemical coordination.

A new intermediate phase adduct (SnI_2·DMSO·MAFa) was first developed by using ionic liquid to construct high-quality tin perovskite films for highly stable, lead-free perovskite solar cells. MAFa was added in the tin perovskite precursor to form a stable SnI_2·DMSO·MAFa adduct, thereby modulating the tin perovskite crystallization and precluding the SnI_2 clusters formation. The residual MAFa was bonded to iodide ion vacancies and uncoordinated Sn^{2+} of tin perovskite film at the grain boundaries to suppress the oxidation of Sn^{2+}. The high-quality films resulted in significantly improved device performance with PCE over 10%. The MAFa-derived devices maintained ∼80% of the initial efficiency over 2800 h of storage under N_2 containing 50−100 ppm of O_2. We believe that the proposed intermediate phase adduct approach are very promising for the fabrication of high-quality tin perovskite films, providing a methodological base to further enhance stability of TPSCs.

■ ASSOCIATED CONTENT

Supporting Information

The Supporting Information is available free of charge at https://pubs.acs.org/doi/10.1021/acsmaterialslett.3c00340.

All details including materials; synthesis of MAFa ionic liquid; synthesis of intermediate phase adduct powders and characterization; chemical structure of MAFa; time-dependent photographs; heating aging experiment; EPS of MAFa; ^{1}H-NMR spectra; XRD pattern of perovskite films; the absorption spectra and tauc plots of perovskite films; air aging experiment; FTIR spectra of perovskite; SEM grain size distribution; device structure of TPSCs; the statistics of V_{oc}, J_{sc}, and FF distribution; normalized V_{oc}, J_{sc}, and FF stability; normalized PCE of the unencapsulated devices under air condition; water contact angle of control and MAFa-derived perovskite films; dark current of control and MAFa-derived TPSCs; SCLC analysis of control and MAFa-derived devices; table of photovoltaic parameter of the devices under reverse and forward scans (PDF)

■ AUTHOR INFORMATION

Corresponding Authors

Ligang Xu − *Key Laboratory for Organic Electronics and Information Displays (KLOEID) & Jiangsu Key Laboratory for Biosensors, Institute of Advanced Materials (IAM), Nanjing University of Posts & Telecommunications, Nanjing 210023, China; Wuhan National Laboratory for Optoelectronics, Huazhong University of Science and Technology, Wuhan 430074 Hubei, China;* orcid.org/0000-0002-9414-0674; Email: iamlgxu@njupt.edu.cn

Yonghua Chen − *Key Laboratory of Flexible Electronics (KLOFE) & Institute of Advanced Materials (IAM), School of Flexible Electronics (Future Technologies), Nanjing Tech University (NanjingTech), Nanjing 211816, China;* orcid.org/0000-0002-9694-4246; Email: iamyhchen@njtech.edu.cn

Runfeng Chen − *Key Laboratory for Organic Electronics and Information Displays (KLOEID) & Jiangsu Key Laboratory for Biosensors, Institute of Advanced Materials (IAM), Nanjing University of Posts & Telecommunications, Nanjing 210023, China;* orcid.org/0000-0003-0222-0296; Email: iamrfchen@njupt.edu.cn

Authors

Yuhan Zhou − *Key Laboratory for Organic Electronics and Information Displays (KLOEID) & Jiangsu Key Laboratory for Biosensors, Institute of Advanced Materials (IAM), Nanjing University of Posts & Telecommunications, Nanjing 210023, China*

Dongdong Yan − *Key Laboratory for Organic Electronics and Information Displays (KLOEID) & Jiangsu Key Laboratory for Biosensors, Institute of Advanced Materials (IAM), Nanjing University of Posts & Telecommunications, Nanjing 210023, China*

Han Zhang − *Key Laboratory for Organic Electronics and Information Displays (KLOEID) & Jiangsu Key Laboratory for Biosensors, Institute of Advanced Materials (IAM), Nanjing University of Posts & Telecommunications, Nanjing 210023, China*

Yi Jing − *Key Laboratory for Organic Electronics and Information Displays (KLOEID) & Jiangsu Key Laboratory for Biosensors, Institute of Advanced Materials (IAM), Nanjing University of Posts & Telecommunications, Nanjing 210023, China*

Linfeng Chao − *Key Laboratory of Flexible Electronics (KLOFE) & Institute of Advanced Materials (IAM), School of Flexible Electronics (Future Technologies), Nanjing Tech University (NanjingTech), Nanjing 211816, China; Frontiers Science Center for Flexible Electronics, Institute of Flexible Electronics (IFE), Northwestern Polytechnical University, Xi'an 710072, China*

Mingguang Li − *Key Laboratory for Organic Electronics and Information Displays (KLOEID) & Jiangsu Key Laboratory for Biosensors, Institute of Advanced Materials (IAM), Nanjing University of Posts & Telecommunications, Nanjing 210023, China;* orcid.org/0009-0004-5962-8211

Meicheng Li − *State Key Laboratory of Alternate Electrical Power System with Renewable Energy Sources, School of New Energy, North China Electric Power University, Beijing 102206, China;* orcid.org/0000-0002-0731-741X

Complete contact information is available at: https://pubs.acs.org/10.1021/acsmaterialslett.3c00340

Author Contributions

CRediT: **Yuhan Zhou**, **Runfeng Chen**, and **Ligang Xu** conceptualization; **Yuhan Zhou**, **Dongdong Yan**, **Han Zhang** data curation; **Yuhan Zhou**, **Yi Jing**, and **Lingfeng Chao** formal analysis; **Yuhan Zhou**, **Dongdong Yan**, and **Mingguang Li** investigation; **Yuhan Zhou**, **Han Zhang**, **Ligang Xu** methodology; **Yuhan Zhou** visualization; **Ligang Xu**, **Runfeng Chen**, **Meicheng Li**, and **Yuhan Zhou** writing-original draft.

Notes

The authors declare no competing financial interest.

■ ACKNOWLEDGMENTS

This study was supported in part by the National Natural Science Foundation of China (62274094, 22075149, 51972110), Natural Science Foundation of Jiangsu Higher Education Institutions (22KJB510011), the State Key Laboratory of Alternate Electrical Power System with Renewable Energy Sources (LAPS22006), the Open Project Program of Wuhan National Laboratory for Optoelectronics

https://doi.org/10.1021/acsmaterialslett.3c00340
ACS Materials Lett. 2023, 5, 2096−2103

(2020WNLOKF012), Jiangsu Provincial Government Scholarship for Overseas Studies, Beijing Natural Science Foundation (2222076), Huali Talents Program of Nanjing University of Posts and Telecommunications.

REFERENCES

(1) Xu, L.; Wu, D.; Lv, W.; Xiang, Y.; Liu, Y.; Tao, Y.; Yin, J.; Qian, M.; Li, P.; Zhang, L.; Chen, S.; Mohammed, O. F.; Bakr, O. M.; Duan, Z.; Chen, R.; Huang, W. Resonance-Mediated Dynamic Modulation of Perovskite Crystallization for Efficient and Stable Solar Cells. *Adv. Mater.* **2022**, *34*, 2107111.

(2) Lv, W.; Hu, Z.; Qiu, W.; Yan, D.; Li, M.; Mei, A.; Xu, L.; Chen, R. Constructing Soft Perovskite-Substrate Interfaces for Dynamic Modulation of Perovskite Film in Inverted Solar Cells with Over 6200 h Photostability. *Adv. Sci.* **2022**, *9*, 2202028.

(3) Tan, S.; Huang, T.; Yavuz, I.; Wang, R.; Yoon, T. W.; Xu, M.; Xing, Q.; Park, K.; Lee, D. K.; Chen, C. H.; Zheng, R.; Yoon, T.; Zhao, Y.; Wang, H. C.; Meng, D.; Xue, J.; Song, Y. J.; Pan, X.; Park, N. G.; Lee, J. W.; Yang, Y. Stability-limiting heterointerfaces of perovskite photovoltaics. *Nature* **2022**, *605*, 268−273.

(4) Jiang, Q.; Tong, J.; Xian, Y.; Kerner, R. A.; Dunfield, S. P.; Xiao, C.; Scheidt, R. A.; Kuciauskas, D.; Wang, X.; Hautzinger, M. P.; Tirawat, R.; Beard, M. C.; Fenning, D. P.; Berry, J. J.; Larson, B. W.; Yan, Y.; Zhu, K. Surface reaction for efficient and stable inverted perovskite solar cells. *Nature* **2022**, *611*, 278−283.

(5) McMeekin, D. P.; Holzhey, P.; Furer, S. O.; Harvey, S. P.; Schelhas, L. T.; Ball, J. M.; Mahesh, S.; Seo, S.; Hawkins, N.; Lu, J.; Johnston, M. B.; Berry, J. J.; Bach, U.; Snaith, H. J. Intermediate-phase engineering via dimethylammonium cation additive for stable perovskite solar cells. *Nat. Mater.* **2023**, *22*, 73−83. Park, J.; Kim, J.; Yun, H. S.; Paik, M. J.; Noh, E.; Mun, H. J.; Kim, M. G.; Shin, T. J.; Seok, S. I. Controlled growth of perovskite layers with volatile alkylammonium chlorides. *Nature* **2023**, *616*, 724−730.

(6) Li, J.; Cao, H. L.; Jiao, W. B.; Wang, Q.; Wei, M.; Cantone, I.; Lu, J.; Abate, A. Biological impact of lead from halide perovskites reveals the risk of introducing a safe threshold. *Nat. Commun.* **2020**, *11*, 310.

(7) Noel, N. K.; Stranks, S. D.; Abate, A.; Wehrenfennig, C.; Guarnera, S.; Haghighirad, A.-A.; Sadhanala, A.; Eperon, G. E.; Pathak, S. K.; Johnston, M. B.; Petrozza, A.; Herz, L. M.; Snaith, H. J. Lead-free organic−inorganic tin halide perovskites for photovoltaic applications. *Energy Environ. Sci.* **2014**, *7*, 3061−3068.

(8) Yu, B. B.; Chen, Z.; Zhu, Y.; Wang, Y.; Han, B.; Chen, G.; Zhang, X.; Du, Z.; He, Z. Heterogeneous 2D/3D Tin-Halides Perovskite Solar Cells with Certified Conversion Efficiency Breaking 14. *Adv. Mater.* **2021**, *33*, 2102055.

(9) Wang, C.; Zhang, Y.; Gu, F.; Zhao, Z.; Li, H.; Jiang, H.; Bian, Z.; Liu, Z. Illumination Durability and High-Efficiency Sn-Based Perovskite Solar Cell under Coordinated Control of Phenylhydrazine and Halogen Ions. *Matter* **2021**, *4*, 709.

(10) Jia, W.; Wei, Z.; Liu, B.; Yan, D.; Huang, Y.; Li, M.; Tao, Y.; Chen, R.; Xu, L. Dopamine Hydrochloride-Assisted Synergistic Modulation of Perovskite Crystallization and Sn^{2+} Oxidation for Efficient and Stable Lead-free Solar Cells. *ACS Appl. Mater. Interfaces* **2022**, *14*, 46801−46808.

(11) Xu, L.; Zhang, C.; Feng, X.; Lv, W.; Huang, Z.; Lv, W.; Zheng, C.; Xing, G.; Huang, W.; Chen, R. Vapor incubation of $FASnI_3$ films for efficient and stable lead-free inverted perovskite solar cells. *J. Mater. Chem. A* **2021**, *9*, 16943−16951.

(12) Zhou, Y.; Feng, X.; Zhu, J.; Xu, L.; Chen, R. Preparation and Stability Strategies of Inverted Tin-Based Perovskite Solar Cells. *Chin. J. Inorg. Chem.* **2022**, *38*, 1889−1907.

(13) Xu, L.; Feng, X.; Jia, W.; Lv, W.; Mei, A.; Zhou, Y.; Zhang, Q.; Chen, R.; Huang, W. Recent advances and challenges of inverted lead-free tin-based perovskite solar cells. *Energy Environ. Sci.* **2021**, *14*, 4292−4317.

(14) Liu, G.; Zhong, Y.; Feng, W.; Yang, M.; Yang, G.; Zhong, J. X.; Tian, T.; Luo, J. B.; Tao, J.; Yang, S.; Wang, X. D.; Tan, L.; Chen, Y.; Wu, W. Q. Multidentate Chelation Heals Structural Imperfections for Minimized Recombination Loss in Lead-Free Perovskite Solar Cells. *Angew. Chem., Int. Ed.* **2022**, *61*, 202209464.

(15) Di Girolamo, D.; Pascual, J.; Aldamasy, M. H.; Iqbal, Z.; Li, G.; Radicchi, E.; Li, M.; Turren-Cruz, S.-H.; Nasti, G.; Dallmann, A.; De Angelis, F.; Abate, A. Solvents for Processing Stable Tin Halide Perovskites. *ACS Energy Lett.* **2021**, *6*, 959−968.

(16) Zhang, Z.; Kamarudin, M. A.; Baranwal, A. K.; Kapil, G.; Sahamir, S. R.; Sanehira, Y.; Chen, M.; Wang, L.; Shen, Q.; Hayase, S. Sequential Passivation for Lead-Free Tin Perovskite Solar Cells with High Efficiency. *Angew. Chem., Int. Ed.* **2022**, *61*, 202210101.

(17) Liao, Y.; Liu, H.; Zhou, W.; Yang, D.; Shang, Y.; Shi, Z.; Li, B.; Jiang, X.; Zhang, L.; Quan, L. N.; Quintero-Bermudez, R.; Sutherland, B. R.; Mi, Q.; Sargent, E. H.; Ning, Z. Highly Oriented Low-Dimensional Tin Halide Perovskites with Enhanced Stability and Photovoltaic Performance. *J. Am. Chem. Soc.* **2017**, *139*, 6693−6699.

(18) Xiang, W.; Zhang, J.; Liu, S.; Albrecht, S.; Hagfeldt, A.; Wang, Z. Intermediate phase engineering of halide perovskites for photovoltaics. *Joule* **2022**, *6*, 315−339.

(19) Wu, T.; Liu, X.; Luo, X.; Lin, X.; Cui, D.; Wang, Y.; Segawa, H.; Zhang, Y.; Han, L. Lead-free tin perovskite solar cells. *Joule* **2021**, *5*, 863−886.

(20) Wu, T.; Liu, X.; He, X.; Wang, Y.; Meng, X.; Noda, T.; Yang, X.; Han, L. Efficient and stable tin-based perovskite solar cells by introducing π-conjugated Lewis base. *Sci. China Chem.* **2020**, *63*, 107−115.

(21) Hao, F.; Stoumpos, C. C.; Guo, P.; Zhou, N.; Marks, T. J.; Chang, R. P.; Kanatzidis, M. G. Solvent-Mediated Crystallization of $CH_3NH_3SnI_3$ Films for Heterojunction Depleted Perovskite Solar Cells. *J. Am. Chem. Soc.* **2015**, *137*, 11445−11452.

(22) Jiang, X.; Li, H.; Zhou, Q.; Wei, Q.; Wei, M.; Jiang, L.; Wang, Z.; Peng, Z.; Wang, F.; Zang, Z.; Xu, K.; Hou, Y.; Teale, S.; Zhou, W.; Si, R.; Gao, X.; Sargent, E. H.; Ning, Z. One-Step Synthesis of SnI_2.$(DMSO)_x$ Adducts for High-Performance Tin Perovskite Solar Cells. *J. Am. Chem. Soc.* **2021**, *143*, 10970.

(23) Saidaminov, M. I.; Spanopoulos, I.; Abed, J.; Ke, W.; Wicks, J.; Kanatzidis, M. G.; Sargent, E. H. Conventional Solvent Oxidizes Sn(II) in Perovskite Inks. *ACS Energy Lett.* **2020**, *5*, 1153−1155.

(24) Wang, J.; Gao, Z.; Yang, J.; Lv, M.; Chen, H.; Xue, D. J.; Meng, X.; Yang, S. Controlling the Crystallization Kinetics of Lead-Free Tin Halide Perovskites for High Performance Green Photovoltaics. *Adv. Energy Mater.* **2021**, *11*, 2102131.

(25) Li, G.; Su, Z.; Li, M.; Yang, F.; Aldamasy, M. H.; Pascual, J.; Yang, F.; Liu, H.; Zuo, W.; Di Girolamo, D.; Iqbal, Z.; Nasti, G.; Dallmann, A.; Gao, X.; Wang, Z.; Saliba, M.; Abate, A. Ionic Liquid Stabilizing High-Efficiency Tin Halide Perovskite Solar Cells. *Adv. Energy Mater.* **2021**, *11*, 2101539.

(26) Dong, H.; Ran, C.; Li, W.; Liu, X.; Gao, W.; Xia, Y.; Chen, Y.; Huang, W. Reductive ionic liquid-mediated crystallization for enhanced photovoltaic performance of Sn-based perovskite solar cells. *Sci. China Chem.* **2022**, *65*, 1895−1902.

(27) Liu, X.; Wang, Y.; Xie, F.; Yang, X.; Han, L. Improving the Performance of Inverted Formamidinium Tin Iodide Perovskite Solar Cells by Reducing the Energy-Level Mismatch. *ACS Energy Lett.* **2018**, *3*, 1116−1121.

(28) Sun, Y.; Wang, X.; Wang, H. Y.; Yuan, S.; Wang, Y.; Ai, X. C.; Zhang, J. P. Lewis Base-Mediated Perovskite Crystallization as Revealed by In Situ, Real-Time Optical Absorption Spectroscopy. *J. Phys. Chem. Lett.* **2021**, *12*, 5357−5362.

(29) Lee, J. W.; Dai, Z.; Lee, C.; Lee, H. M.; Han, T. H.; De Marco, N.; Lin, O.; Choi, C. S.; Dunn, B.; Koh, J.; Di Carlo, D.; Ko, J. H.; Maynard, H. D.; Yang, Y. Tuning Molecular Interactions for Highly Reproducible and Efficient Formamidinium Perovskite Solar Cells via Adduct Approach. *J. Am. Chem. Soc.* **2018**, *140*, 6317−6324.

(30) Walker, B.; Kim, G. H.; Kim, J. Y. Pseudohalides in Lead-Based Perovskite Semiconductors. *Adv. Mater.* **2019**, *31*, 1807029.

(31) Mahmoudi, T.; Kohan, M.; Rho, W. Y.; Wang, Y.; Im, Y. H.; Hahn, Y. B. Tin-Based Perovskite Solar Cells Reach Over 13% with Inclusion of N-Doped Graphene Oxide in Active, Hole-Transport, and Interfacial Layers. *Adv. Energy Mater.* **2022**, *12*, 2201977.

https://doi.org/10.1021/acsmaterialslett.3c00340
ACS Materials Lett. 2023, 5, 2096−2103

(32) Hao, F.; Stoumpos, C. C.; Cao, D. H.; Chang, R. P. H.; Kanatzidis, M. G. Lead-free solid-state organic−inorganic halide perovskite solar cells. *Nat. Photonics* **2014**, *8*, 489−494.
(33) Li, P.; Dong, H.; Xu, J.; Chen, J.; Jiao, B.; Hou, X.; Li, J.; Wu, Z. Ligand Orientation-Induced Lattice Robustness for Highly Efficient and Stable Tin-Based Perovskite Solar Cells. *ACS Energy Lett.* **2020**, *5*, 2327−2334.
(34) Wang, S.; Yao, H.; Zhu, W.; Wu, C.; Tang, Z.; Liu, J.; Ding, L.; Hao, F. Stabilization of Perovskite Lattice and Suppression of Sn^{2+}/Sn^{4+} Oxidation via Formamidine Acetate for High Efficiency Tin Perovskite Solar Cells. *Adv. Funct. Mater.* **2023**, *33*, 2215041.
(35) Wan, Z.; Ren, S.; Lai, H.; Jiang, Y.; Wu, X.; Luo, J.; Wang, Y.; He, R.; Chen, Q.; Hao, X.; Wang, Y.; Wu, L.; Constantinou, I.; Zhang, W. H.; Zhang, J.; Zhao, D. Suppression of Nonradiative Recombination by Vacuum-Assisted Process for Efficient Lead-Free Tin Perovskite Solar Cells. *Adv. Mater. Interfaces* **2021**, *8*, 2100135.
(36) Zhou, Y.; Yan, D.; Feng, X.; Shen, B.; Yang, L.; Wang, J.; Chen, R.; Lv, W.; Xu, L. Buried Interface Modification via Guanidine Thiocyanate for High-Performance Lead-Free Perovskite Solar Cells. *J. Phys. Chem. C* **2023**, *127*, 1320−1325.

https://doi.org/10.1021/acsmaterialslett.3c00340
ACS Materials Lett. 2023, 5, 2096−2103